

ACCEPTED MANUSCRIPT

Three-dimensional localization at the nanometer scale and thermal sensing of living cells

To cite this article before publication: Jun Yang *et al* 2019 *J. Phys. D: Appl. Phys.* in press <https://doi.org/10.1088/1361-6463/ab284f>

Manuscript version: Accepted Manuscript

Accepted Manuscript is “the version of the article accepted for publication including all changes made as a result of the peer review process, and which may also include the addition to the article by IOP Publishing of a header, an article ID, a cover sheet and/or an ‘Accepted Manuscript’ watermark, but excluding any other editing, typesetting or other changes made by IOP Publishing and/or its licensors”

This Accepted Manuscript is © 2019 IOP Publishing Ltd.

During the embargo period (the 12 month period from the publication of the Version of Record of this article), the Accepted Manuscript is fully protected by copyright and cannot be reused or reposted elsewhere.

As the Version of Record of this article is going to be / has been published on a subscription basis, this Accepted Manuscript is available for reuse under a CC BY-NC-ND 3.0 licence after the 12 month embargo period.

After the embargo period, everyone is permitted to use copy and redistribute this article for non-commercial purposes only, provided that they adhere to all the terms of the licence <https://creativecommons.org/licenses/by-nc-nd/3.0>

Although reasonable endeavours have been taken to obtain all necessary permissions from third parties to include their copyrighted content within this article, their full citation and copyright line may not be present in this Accepted Manuscript version. Before using any content from this article, please refer to the Version of Record on IOPscience once published for full citation and copyright details, as permissions will likely be required. All third party content is fully copyright protected, unless specifically stated otherwise in the figure caption in the Version of Record.

View the [article online](#) for updates and enhancements.

Three-dimensional Localization at the Nanometer Scale and Thermal sensing of Living Cells

Jun Yang^{1, 3*}, Zheng Ling^{1, 3}, Rongheng Li², Xuesong Mei^{1, 3},

¹State Key Laboratory for Manufacturing Systems Engineering, Xi'an Jiaotong University, Xi'an, 710049, China

²Department of Mechanical Engineering, College of Engineering and Computer Science, University of Michigan, MI 48128, USA

³Shaanxi Key Laboratory of Intelligent Robots, Xi'an Jiaotong University, Xi'an, 710049, China

E-mail address: softyj@xjtu.edu.cn, softyj@163.com

Abstract: Despite the fact that the theory and application of particle three-dimensional localization have been studied extensively, it is still difficult to apply this technique to 3D measurements of temperature field distribution of cells at the micro-nano scale. In this study, an optical system exhibiting double helix point spread function (DH-PSF) was developed based on the properties of vortex beams, which is suitable for examining particle 3D localization at nanometer scale. Then calibration was performed along the axial and transverse dimensions. The measurement range was $133 \times 133 \times 1.36 \mu\text{m}^3$, and the spatial resolution was about 140 nm. Combining with QD fluorescence thermometry, a 3D positioning and temperature measurement method for living cells is proposed. The system was applied into temperature field measurement for living cells. For the first time, we realized three-dimensional positioning and temperature measurement of quantum dot probes at nanoscale and reconstructed the temperature field of cells. The experimental results of cells show that the measurement system fulfilled 3D localization requirements and could be used to measure the temperature of QDs. Based on the experiment, we draw a schematic diagram of the temperature field distribution of tumor cells. The method proposed in this paper offers an effective tool for studying the dynamics of nanoparticles in complex environments and for studying thermal field variations caused by cytopathic diseases.

Keywords: vortex beam, double helix point spread function, nano-scale 3D positioning, quantum dot, temperature field distribution of cells

1. Introduction

Accurate position localization at the micro-nano scale, which is a prerequisite for manipulating nanomaterials, is a grand challenge at present. Micro-nano scale heat generation and transmission under unconventional conditions is directly related to material properties and cell metabolism, especially in lesions. In order to explore and improve the physicochemical properties of new materials at the micro-nano scale and perform accurate intracellular imaging and temperature gradient measurements, researchers in various fields yearn for a powerful nanoscale 3D localization and temperature measurement tool. This is of particular significance in biology. As the key driver of metabolism, a temperature gradient exists inside cells as metabolic activities are not evenly distributed within a cell. Through accurate 3D temperature measurement at the micro-nano scale, researchers can establish the relationship between local heat generation and metabolic processes, which allows them to identify the causes of various diseases.

Many methods have been developed for use in the field of 3D particle localization. Among them, confocal microscopy, defocus imaging positioning, and DH-PSF are particular areas of interest. As a microscopy technique developed in recent years, confocal microscopy has found uses in cytology, microbiology, genetics, neurobiology, physiology, and pathology, becoming an indispensable tool in modern biology. Mathai et al. summarized the existing 3D particle tracking methods and pointed out potential future development and application prospects.^[1] Shen summarize the algorithms behind, and practical applications of single particle tracking (SPT).^[2] Beaune et al.^[3] embedded QDs into giant vesicles and used fibre-optic fluorescence confocal microscopy for 3D tracking, thus paving the way for high heat therapy for tumours. Bon combined SELFIE with conventional localization microscopy to visualize F-actin 3D filament networks and reveal the spatial distribution of the transcription factor OCT4 in human induced pluripotent stem cells at depths up to 50 μm inside uncleared tissue spheroids.^[4]

Moreover, Smoyer adapted split green fluorescent protein (split-GFP) to

systematically localize known and predicted integral membrane proteins in *Saccharomyces cerevisiae* to the INM as opposed to the outer nuclear membrane.^[5] Liu developed a novel design of activity localization fluorescence (ALF) peptide probe, which enables spatially resolved, highly sensitive imaging of peptidase in living cells.^[6] Johnson detected single molecules of CaM labelled with a fluorescent dye and injected into living HEK 293 cells, and used high-speed, wide-field, single-molecule imaging to track single CaM molecules.^[7] Ballister presented a new technique to rapidly and reversibly control protein localization in living cells with subcellular spatial resolution using a cell-permeable, photoactivatable chemical inducer of dimerization.^[8]

Nathan^[9] used confocal microscopy to study spatial localization and tracking of single QDs against a high-brightness background. An excited-state intramolecular proton transfer (ESIPT)-based solid-state fluorophore HTPQ was developed that is further utilized in the design of an enzyme-responsive, fluorogenic probe (HTPQA), making possible diffusion-resistant in-situ detection of endogenous ALP in live cells.^[10] Huang described an RNA-based fluorescent sensor for small RNA detection both in vitro and in vivo, adaptable for any small RNA, demonstrating its potential for tracking miRNA expression and localization in vivo.^[11] On the basis of confocal microscopy, Hu^[12] used a near-infrared laser as a light source to perform 3D localization and tracking of gold nanoparticles in low illumination conditions, achieving a spatial resolution of up to 210 nm and a response time of less than 1 ms. When conducting measurements using confocal microscopy, only a single point in space is measured at a time. If the aim is to measure an entire space, it is necessary to move the objective or employ a raster scanning mechanism to gather point-by-point measurements.

When using conventional microscopic imaging systems to estimate the positions of particles, two issues need to be considered: a) transverse measurement, i.e., measurement in the XY plane perpendicular to the optical axis; b) axial measurement, i.e., measurement of displacement along the optical axis (Z-direction). At present,

there are relatively mature transverse measurement techniques available for accurate localization, such as the centroid, Hough transformation, gradient methods.^[13] Most methods for measuring small displacements along the axial direction are based on defocus imaging. Speidel^[14] first proposed the use of defocus imaging to measure the axial displacement of particles in 2003, and Zhang^[15-18] later conducting significant research in this area.

The defocus imaging method is based on the idea of matching the defocus distances with image features generated when particles are at different positions relative to the focal plane of the objective lens. The researchers installed porous masks in the microscopic imaging systems to study the relationship between the spacing between image spots and the defocus distance, thus enabling positioning along the optical axis. Pereria^[19] established and analysed a defocus imaging model featuring a three-hole mask in 2001. The three-hole mask could be used to convert the axial distance of the particles into the spacing between three spots. However, the overall light energy utilization of the system was relatively low due as the three-hole mask blocked some light, making it unsuitable for low-light imaging.

An imaging system exhibiting DH-PSF captures images of a particle in the form of a spot pair whose central position is used for transverse positioning of the particle. When the particle deviates from the focal plane of the objective lens, the spot pair rotates around its center and stops at an angle determined by the defocus distance. By matching the refractive index of the objective lens immersion liquid to that of the sample media, Carr demonstrate DHPSF imaging of up to 15- μ m-thick whole eukaryotic cell volumes in three to five imaging planes.^[20] Pavani et al.^[21] applied DH-PSF to wide-field microscopy for super-resolution imaging of single-molecule fluorescence and high-resolution 3D localization of fluorescent proteins. Shechtman proposed a 3D localization method based on a quadrilateral PSF, which enabled observation of chromatin dynamics in cells.^[22] Thompson et al.^[23] applied DH-PSF to wide-field microscopy to enable high-resolution 3D tracking of mRNA.

According to the operational principle of confocal microscopy, localization of

particles within a particular space requires point-by-point scanning of the entire space. The localization efficiency is low when the number of particles in the space being measured is small. In contrast, defocus imaging microscopy and the DH-PSF method can be used to obtain position information of all particles in the space in one measurement, resulting in high localization efficiency. The hardware design of a defocus imaging system is relatively simple, and the particles are localized by the matching algorithm, while the DH-PSF method offers higher sensitivity.^[24]

Although the above methods can locate particles in space, they cannot simultaneously measure the temperature of particles at nanoscale.

The temperature measurement technique is indispensable in intracellular 3D temperature measurements. QDs are favoured by researchers due to their desirable physical properties, such as their small size and adjustable band gap. QD applications include QD biomarkers ^[25-26], QD solar cells^[27], QD displays^[28], and QD light-emitting diodes.^[29] Liu developed a new graphene QD fluorescent nanosensor for detecting nitrite in living cells.^[30] Mu used QDs to measure cytotoxicity.^[31] Ma describe a strategy for live cell imaging of single genomic loci by combining transcription activator-like effectors (TALEs) with a QD labelling technique.^[32]

In the area of temperature measurements in microelectronic components, Choudhury ^[33] used QDs to enable local thermal imaging of photofluidic devices. Devin ^[34] used functional mapping between the peak wavelength and temperature of CdSe/ZnS QDs in the 295~525 K temperature range by doping CdSe/ZnS core-shell QDs with SiO₂, enabling temperature monitoring over a wider range. Li ^[35] used CdSe/ZnS QDs to characterize Joule heating in MEMS microstructures.

However, the above research on temperature measurements using QDs has reached an advanced stage in terms of depth and breadth, they can only measure the plane or surface 2D temperature of cells, while could not provide an intracellular three-dimensional temperature distribution map. More effort must focus on the use of QDs for 3D temperature measurements of living cells at the micro-nano scale.

In summary, although much research has been conducted in the area of 3D

temperature distribution measurements (e.g., fabrication and application of QD temperature probes, and particle localization methods), researchers still have not found a DH-PSF suitable for intracellular 3D temperature distribution measurements at the micro-nano scale, nor have they found a method for determining the physical parameters of the experimental bench.

3D temperature measurements at the micro-nano scale play a crucial role in life science research and other areas, but the existing temperature measurement techniques cannot meet the requirements. In this study, effort was made to develop a new micro-nano scale temperature measurement method which uses QDs as the temperature probe and uses a DH-PSF-based probe positioning mechanism. The theoretical basis for axial positioning was established by analyzing the formation of the DF-PSF. A mathematical physics model of the imaging system was constructed; the DF-PSF was designed by determining the appropriate set of parameters, and the system was verified in experiment. A system combining QD temperature measurements with 3D localization was designed and calibrated. Finally, an experiment was designed to measure the temperature and spatial position of a QD simultaneously with the aim of verifying the effectiveness of the proposed measurement method. The system has been applied in the field of cell temperature measurement. It is the first time to realize reconstruction of cell temperature field.

2. Design of Axial Positioning DH-PSF

2.1. Defocus double helix

Maxwell's equations are a set of coupled partial differential equations that describe the relationship between the electric field, magnetic field, charge density, and current density. In free space without a charge or current distribution, Maxwell's equations can be transformed to obtain an elliptic partial differential equation that governs monochromatic electromagnetic waves, namely the Helmholtz equation. The basic form of the Helmholtz equation is as follows:

$$(\nabla^2 + k^2)A = 0 \quad (1)$$

where ∇^2 is the Laplace operator, k is wavenumber ($\text{rad}\cdot\text{m}^{-1}$), and A is the electric field ($\text{N}\cdot\text{C}^{-1}$).

Equation (1) can be approximated as a complex amplitude U as a function of the z coordinate for paraxial waves. The paraxial form of the Helmholtz equation is as follows:

$$\left(\frac{\partial^2}{\partial x^2} + \frac{\partial^2}{\partial y^2}\right)U - 2ik \frac{\partial U}{\partial z} = 0 \quad (2)$$

Where U is the complex amplitude ($\text{N}\cdot\text{C}^{-1}$) and i is the imaginary constant.

The simplest solution to the paraxial Helmholtz equation is in the form of a paraxial spherical wave, i.e., a Gaussian beam. Solving the paraxial Helmholtz equation in cylindrical coordinates can produce another set of complete solutions, which can be written as the product of Laguerre polynomials and a Gaussian function (i.e. the Laguerre-Gaussian beam).^[36]

$$u_{mn}(r) = G(r, z) R_{mn}(r) Z_{mn}(z) \phi_m(\theta) \quad (3)$$

Among the elements that make up Eq. (3), $G(r, z)$ is the a function describing a travelling Gaussian beam, and the remaining factors are related to Laguerre polynomials. Each element can be expanded as follows:

$$\begin{aligned} G(r, z) &= \frac{w(0)}{w(z)} \exp\left(-\frac{r^2}{w^2(z)}\right) \exp\left(-\frac{ikr^2}{2R(z)}\right) \exp\left(\tan^{-1}\left(\frac{z}{z_R}\right)\right) \exp(-ikz) \\ R_{mn}(r) &= \left(\frac{\sqrt{2}r}{w(z)}\right)^2 L_n^m\left(\frac{2r^2}{w^2(z)}\right) \\ Z_{mn}(z) &= \exp\left(i(2m+n)\tan^{-1}\left(\frac{z}{z_R}\right)\right) \\ \phi_m(\theta) &= \exp(im\theta) \end{aligned} \quad (4)$$

where $w(z)$ is the width of beam/m, $R(z)$ is the wavefront radius of curvature (m), z_R is the Rayleigh distance (m), and $L_n^m(x)$ is a Laguerre polynomial.

The linearity of the Helmholtz equation allows the solution to be rewritten as a superposition of different Laguerre-Gaussian beams. Assuming that the constituent

beams of a composite wave have the same parameters, except for the Laguerre mode, the composite wave can be described by:

$$u(r) = \sum_{j=1}^Q A_j u_{m_j, n_j}(r) \quad (5)$$

where A_j is the weight of mode j .

Without loss of generality, assuming that the selected Laguerre-Gaussian mode satisfies $n_j < n_j + 1$, the intensity of the light field at any point during beam propagation can be expressed as:

$$\begin{aligned} I(r) &= u(r) u^*(r) \\ &= |G(r, z)|^2 \left\{ \sum_{j=1}^Q |A_j|^2 R_{m_j, n_j}^2(r) + \sum_{j=1}^Q \sum_{p=j+1}^Q 2|A_j||A_p| R_{m_j, n_j}(r) R_{m_p, n_p}(r) \right. \\ &\quad \left. \times \cos \left[\Delta m_{jp} \theta - \Delta n_{jp} \tan^{-1} \left(\frac{z}{z_R} \right) - \phi_{jp} \right] \right\} \end{aligned} \quad (6)$$

where: $\Delta m_{jp} = m_j - m_p$; $\Delta n_{jp} = n_j - n_p$; $\phi_{jp} = \arg(A_j) - \arg(A_p)$.

When two points in the space $P_1(r_1, \theta_1, z_1)$ and $P_2(r_2, \theta_2, z_2)$ are in the same propagation plane (i.e., $z_1 = z_2$), the two points have the same intensity (i.e., $I(P_1) = I(P_2)$) if the following equations are satisfied:

$$\begin{aligned} r_1 &= r_2 \\ \Delta m_{jp} \theta_1 - \Delta n_{jp} \tan^{-1} \left(\frac{z_1}{z_R} \right) - \phi_{jp} &= \Delta m_{jp} \theta_2 - \Delta n_{jp} \tan^{-1} \left(\frac{z_2}{z_R} \right) - \phi_{jp} + 2N\pi \\ N &= 0, 1, 2, \dots \end{aligned} \quad (7)$$

Substituting $z_1 = z_2$ into Eq. (7) yields the following:

$$\begin{aligned} r_1 &= r_2 \\ \theta_1 - \theta_2 &= \frac{\Delta n_{jp}}{\Delta m_{jp}} 2N\pi, N = 0, 1, 2, \dots \end{aligned} \quad (8)$$

One can see from Eq. (8) that when $\left| \frac{\Delta n_{jp}}{\Delta m_{jp}} \right|$ is a constant smaller than 1 (i.e., the

Laguerre modes of the constituent beams are on the same slant line), the intensity distribution of the light field in any propagation plane exhibits periodicity during beam propagation, and the minimum positive period is $\left| \frac{\Delta n_{jp}}{\Delta m_{jp}} 2\pi \right|$.

To verify the correctness of this analysis, we wrote a MatLab program to calculate the light field distribution in the propagation plane for $z=0$ and various values of $\left| \frac{\Delta n_{jp}}{\Delta m_{jp}} \right|$. The result is shown in Figure 1. In **(Figure 1a)**, the chosen Laguerre mode set (m, n) is (2, 1), (4, 2), and (6, 3), and the theoretical minimum positive period is π . The chosen Laguerre mode set in **(Figure 2b)** is (4, 1), (8, 2), and (12, 3), and the theoretical minimum positive period is $\frac{\pi}{2}$. The calculated results agree with the theoretical results.

One can see from observing the cosine portion of Eq. (6), the greatest light intensity in any given propagation plane is at the point satisfying the following equation:

$$\cos \left[\Delta m_{jp} \theta - \Delta n_{jp} \tan^{-1} \left(\frac{z_1}{z_R} \right) - \phi_{jp} \right] = 1 \quad (9)$$

Reorganizing Eq. (9) yields:

$$\theta = \frac{\Delta n_{jp} \tan^{-1} \left(\frac{z_1}{z_R} \right) + \phi_{jp} + 2N\pi}{\Delta m_{jp}}, N = 0, 1, 2, \dots \quad (10)$$

One can see the following fact regarding the points $P_1(r_1, \theta_1, z_1)$ and $P_2(r_2, \theta_2, z_2)$ from Eq. (10): if they are not in the same propagation plane and coincide with the highest light intensity in their respective planes, the angle between them is

$$\begin{aligned}
\theta_1 - \theta_2 &= \frac{\Delta n_{jp} \tan^{-1}\left(\frac{z_1}{z_R}\right) + \phi_{jp} + 2N_1\pi}{\Delta m_{jp}} - \frac{\Delta n_{jp} \tan^{-1}\left(\frac{z_2}{z_R}\right) + \phi_{jp} + 2N_2\pi}{\Delta m_{jp}} \\
&= \frac{\Delta n_{jp}}{\Delta m_{jp}} \left(\tan^{-1}\left(\frac{z_1}{z_R}\right) - \tan^{-1}\left(\frac{z_2}{z_R}\right) \right) + \frac{2\Delta N\pi}{\Delta m_{jp}} \quad (11) \\
\Delta N &= 0, 1, 2, \dots
\end{aligned}$$

One can see from the analysis that the light intensity distribution on the beam propagation plane rotates during propagation. Meanwhile, the beam cross section will change due to the influence of $G(r, z)$: the beam cross section at the beam waist is the smallest, and it becomes progressively larger as it moves away from the beam waist.

The point spread function (PSF) is a function describing the ability of an optical system to resolve a point source.^[37] For a typical imaging system shown in **(Figure 1c)**, the PSF can be understood as the corresponding light field distribution in the image plane when there is only a point light source in the object plane.

Assume that the PSF for the imaging system shown in Figure 2 is $h(x_o, y_o, x_i, y_i)$, and the PSF is a superposition of several Laguerre-Gaussian beams:

$$h(x_o, y_o, x_i, y_i) = \sum_{j=1}^Q c_j u_{m_j, n_j}(r, \theta, 0) \quad (12)$$

where x_o, y_o are the object coordinates, x_i, y_i are the image coordinates, c_j is a weight coefficient, and $u_{m_j, n_j}(r, \theta, 0)$ is the light field distribution of a Laguerre-Gaussian beam at $z=0$.

The PSF shown in **(Figure 1a)** corresponds to a Laguerre-Gaussian beam that satisfies $\left| \frac{\Delta n_{jp}}{\Delta m_{jp}} \right| = \frac{1}{2}$. This can be derived from the nature of a vortex beam when the object plane remains stationary and the observation plane deviates from the image plane, thus the light field in the observation plane will rotate. Assume that the offset of the observation plane from the image plane is Δz , as shown in **(Figure 1d)**. The image field distribution can be expressed as follows due to Fresnel diffraction:

$$\delta(x_o, y_o) \otimes h(x_o, y_o, x_i, y_i) \otimes \exp\left[i\pi \frac{x_i^2 + y_i^2}{\lambda \Delta z}\right] \quad (13)$$

where $\delta(x_o, y_o)$ is an impact function, \otimes is the convolution operation, and λ is the wavelength (m).

(Figure 1e) shows that when the object moves along the optical axis and the defocus distance is Δz , the light field distribution on the image plane can be expressed as:

$$\delta(x_o, y_o) \otimes \exp\left[i\pi \frac{x_i^2 + y_i^2}{\lambda \Delta z}\right] \otimes h(x_o, y_o, x_i, y_i) \quad (14)$$

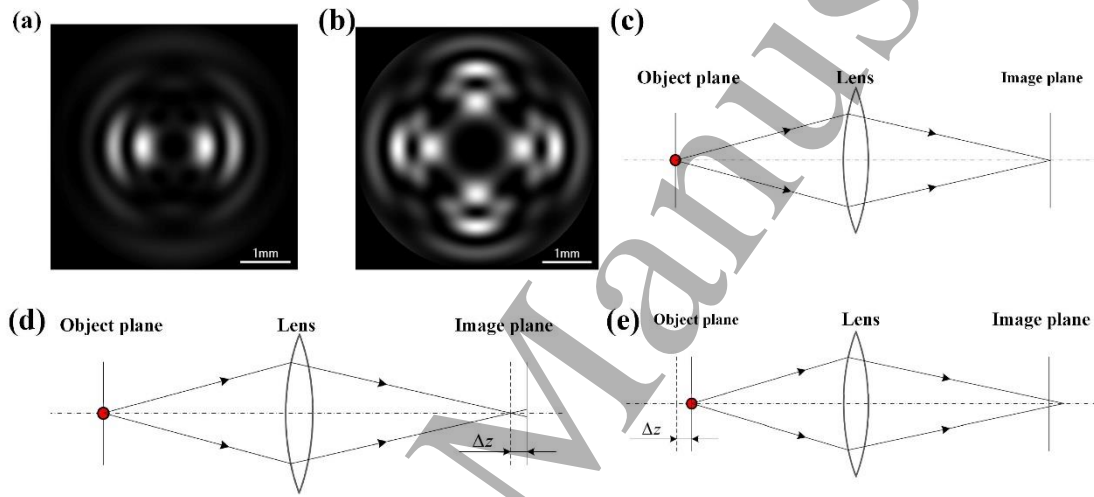


Figure 1. Double helix map of vortex beam. (a) Light field distribution due to superposition of different Laguerre modes: mode set (2, 1) (4, 2) (6, 3), and (b) Mode set (4, 1) (8, 2) (12, 3). (c) A typical imaging system. (d) Defocusing at the image side. (e) Defocusing at the object side.

It is known from the convolution exchange law that Eqs. (13) and (14) are equivalent, i.e., when the observation plane remains stationary and the object point light source is out of focus, the image on the observation plane rotates as the defocus distance changes.

Therefore, the effect of the defocusing double helix can be achieved by choosing the PSF resulting from superposition of a number of Laguerre-Gaussian beams that

satisfy $\left| \frac{\Delta n_{jp}}{\Delta m_{jp}} \right| = \frac{1}{2}.$

2.2. Design of the optical path system and optical field physical model

In the area of optical information processing, the 4f optical system is widely used in optical experiments thanks to its merits, such as simple optical path and less demand on the stability of the light source.^[38] As shown in **(Figure 2a)**, the distance between each plane and the adjacent Fourier transform lens is equal to the focal length of the lens, thus the name “4f system”.

According to Abbe imaging theory, the amplitude distribution on the image plane in a 4f system can be regarded as resulting from the amplitude distribution in the object plane undergoing two rounds of diffractions. The first round is the Fourier transform of the amplitude distribution in the object plane to the Fourier transform spectrum plane. The second time is an inverse Fourier transform from the Fourier transform spectrum plane to the image plane. After the two transformations, the amplitude distribution on the image plane is still the object amplitude function, except that the coordinates are reversed.^[39]

One can see from the characteristics of the 4f system that its PSF is the Fourier transform of the modulation function in the Fourier transform spectrum plane. Considering the fact the Laguerre-Gaussian mode remains unchanged after a Fourier transform^[36], the modulation function of the Fourier transform spectrum plane can be designed as a proper superposition of Laguerre-Gaussian modes. The DH-PSF is obtained in this way.

Setting the axial coordinates in Eqs. (3) and (4) to zero and normalizing yields the Laguerre-Gaussian mode:

$$u_{mn} = \left[\frac{2(n-m)!}{\pi w_0^2 (n!)^3} \right]^{\frac{1}{2}} \exp \left[-\left(\frac{r}{w_0} \right)^2 \right] \left(\sqrt{2} \frac{r}{w_0} \right)^m L_n^m \left[2 \left(\frac{r}{w_0} \right)^2 \right] \exp(im\theta) \quad (15)$$

where w_0 is the beam waist (m).

Let the modulation function $S(r, \theta)$ in the Fourier transform spectrum plane be a superposition of Laguerre-Gaussian modes. In polar coordinates, we have

$$S(r, \theta) = \sum_{i=1}^{\infty} c_i u_{m_i n_i} \quad (16)$$

For the imaging system shown in Figure 5, when light $U_o(x_o, y_o)$ from the object plane propagates to the Fourier transform spectrum plane, the light field distribution in the Fourier transform spectrum plane can be expressed as:

$$U_{spp}(x_{spp}, y_{spp}) = \frac{\exp\left[i \frac{k}{2f} \left(1 - \frac{d}{f}\right) (x_{spp}^2 + y_{spp}^2)\right]}{i\lambda f} \times \iint U_o(x_o, y_o) \exp\left[-i \frac{2\pi}{\lambda f} (x_o x_{spp} + y_o y_{spp})\right] dx_o dy_o \quad (17)$$

where d is the object distance (m).

When the object plane is a point source located on the optical axis, the light field distribution on the object plane can be expressed as an impact function $\delta(x_o, y_o)$. At this time, the light field distribution prior to the Fourier transform spectrum plane is

$$U_{spp}(x_{spp}, y_{spp}) = \frac{\exp\left[i\alpha (x_{spp}^2 + y_{spp}^2)\right]}{i\lambda f} \quad (18)$$

$$\alpha = \frac{k}{2f} \left(1 - \frac{d}{f}\right) = \frac{k\Delta z}{2f^2}$$

Thus, the light field distribution $U_i(x_i, y_i)$ in the image plane can be described by

$$U_i(x_i, y_i) = \frac{1}{i\lambda f} \iint U_{spp}(x_{spp}, y_{spp}) S(x_{spp}, y_{spp}) \times \exp\left[-i \frac{2\pi}{\lambda f} (x_i x_{spp} + y_i y_{spp})\right] dx_{spp} dy_{spp} \quad (19)$$

This concludes the mathematical physics model of the 4f imaging system, and Eq. (19) will serve as a basis for subsequent simulations.

2.3. Parameter design for the axial positioning system

The DH-PSF is designed based on the 4f system shown in (Figure 2a). The design primarily involves determining the parameters for the optical elements in the system (such as lens focal length and clear aperture) and designing the modulation function in the Fourier transform spectrum plane.

Designing the modulation function in the Fourier transform spectrum plane primarily involves two aspects: combining the Laguerre-Gaussian modes (m, n) and the beam waist parameter. The combination of modes directly affects the shape of the system PSF, and the beam width parameter affects the spot size of the image.

Commonly used lens focal lengths are 75 mm, 100 mm, 200 mm, and 300 mm. Selecting a telephoto lens will result in an excessively large system. On the other hand, a focal length that is too short will bring inconvenience to system installation and subsequent adjustment. Considering the commonly used optical design system, the focal length of the lens was designed to be 200 mm. After studying the design of other widely-used optical systems and careful consideration, we decided to adopt a focal length of 200 mm.

In the design of an optical system, the clear aperture is another parameter that must be considered carefully. An excessively small aperture is likely to cause diffraction and reduce image quality. However, choosing an excessively large aperture requires the use of optical components with large apertures, which increases the size of the system and presents a challenge regarding sealing.

In the subsequent design, the axial positioning system must work with the microscope and the imaging CCD. The size of the CCD is usually 5~6mm. After studying the optical system design manual and careful consideration, we decided to use a 7 mm clear aperture.

The combination of Laguerre-Gaussian modes primarily involves two aspects: choosing modes and determining the relative weights of the modes. According to the above mathematical physics model, the imaging system exhibits a defocused double helix when the selected Laguerre-Gaussian modes (m, n) satisfy $\left| \frac{\Delta n_{jp}}{\Delta m_{jp}} \right| = \frac{1}{2}$. Thus, the selected mode set (m, n) was (1, 0), (3, 1), (5, 2), (7, 3), and (9, 4). They were assigned the same weight for design convenience.

The beam waist in Eq. (15) is obtained by calculating the beam widths $w(z)$ in Eqs. (3) and (4) at $z=0$. One can see from Eqs. (15) and (16) that this parameter

affects the effective domain of the modulation function.

As the PSF in the 4f system is the Fourier transform of its spectrum plane modulation function, and the temporal width of the Fourier transform is inversely related to the width of the frequency spectrum, the value of w_0 will affect the imaging size: a larger the value of w_0 results in a smaller the image size.

To study the influence of the parameter w_0 on imaging and determine the appropriate value of w_0 , we set the wavelength of light to 650 nm and calculated the image sizes when w_0 was assigned different values. The results are shown in (Figure 2b).

(Figure 2b) shows the light intensity distribution in the image plane after a point source is projected onto the image plane with the optical system. The values of w_0 corresponding to these images are 0.6, 0.8, 1.0, 1.2, and 1.4 mm from left to right, respectively. The distance between the two brightest points in the two light spots is the spot spacing (see Table 1).

Table 1. Correspondence between spot spacing and beam waist

Beam waist (w_0/mm)	Spot spacing (μm)
0.6	150
0.8	120
1.0	85
1.2	70
1.4	60

A comparison between various spot spacing values and the corresponding beam waist reveals that the image size is inversely related to the beam waist, as shown in (Figure 2b). This is consistent with the theoretical analysis.

In actual imaging systems, the sensors used to acquire images (such as a CCD) are discrete acquisition units, as shown in (Figure 2c). The spot spacing directly affects imaging and the curvature resolution, which in turn affects the axial positioning resolution.

If the end image is so small that its size is approximately a single pixel, the imaging system cannot reproduce the spot pair and the resolution of the rotation angle is low, resulting in low image resolution.

On the other hand, the end image should not be too large. When the end image is too large, part of the image can get lost when the points on the boundary of the field of view are projected on the CCD, resulting in a smaller effective measurement range.

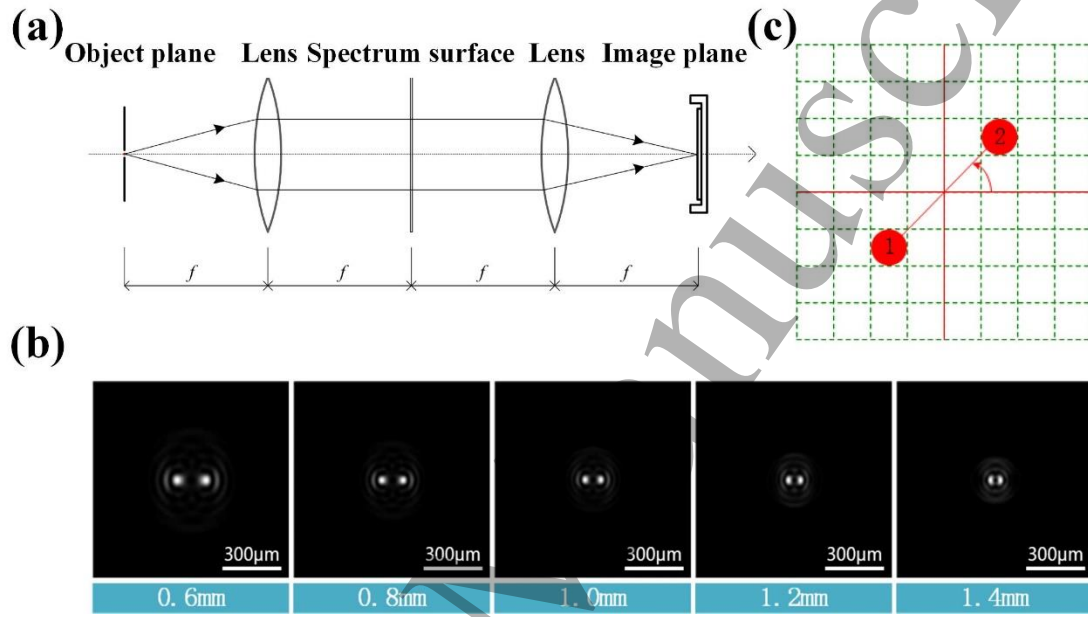


Figure 2. Design of Axial Positioning DH-PSF. (a) A typical 4f system. (b) Influence of w_0 on image size. The values of w_0 corresponding to these images are 0.6, 0.8, 1.0, 1.2, and 1.4 mm from left to right, respectively. (c) Illustration of an imaging sensor.

QDs generally have a size of 10 nm or less; the size of the image after passing a 100x objective lens is about 1 μm , and the pixel size of a common imaging sensor is in the range of 6-13 μm . Considering all the above factors, a spacing of 85 μm can be used when imaging QDs. Therefore, the beam waist should be 1.0 mm.

3. Simulation and experimental verification of DH-PSF

3.1. Numerical simulation of DH-PSF

The modulation function $S(r, \theta)$ of the Fourier transform spectrum plane is calculated using Eqs. (15) and (16), as shown in (Figure 3a-b).

(Figure 3a) shows the amplitude modulation part of the modulation function, i.e., the effect of attenuation on light intensity. The white part shows region with high transmittance, and the black part shows a region with large attenuation. (Figure 3b) shows the phase modulation part of the modulation function, i.e., the spatially resolved phase delay.

A MatLab program was written to solve Eq. (19). The modulation function in (Figure 3a-b) was used by the program to calculate the out-of-focus images corresponding to defocus distance values from -10 mm to +10 mm in 2 mm intervals, as shown in (Figure 3c).

One can see from (Figure 3c) that the image formed by projecting a point source through an imaging system is a spot pair. When the point source moves along the positive direction of the optical axis, the image rotates in a clockwise direction. When axial positioning is performed using the modulation function, the axial positioning range is -8 mm to +8 mm.

The brightest points of the two spots in (Figure 3c) can be connected and the inclination angle of the connecting line can be calculated (counterclockwise direction being positive, clockwise direction being negative). This procedure can be applied to the defocus images shown in (Figure 3d-e) to obtain the spot pair rotation angle corresponding to different defocus distances. The results are plotted in (Figure 3f).

Drawing on the method described by Eq. (11), we can use the inverse tangent function to fit the defocused data, resulting in the following fitting equation:

$$\theta = -2.14802 \times \left(-0.00023277 + \tan^{-1} \left(\frac{\Delta d}{9598.06} \right) \right) \quad (20)$$

where θ is the rotation angle and Δd is defocus distance (m).

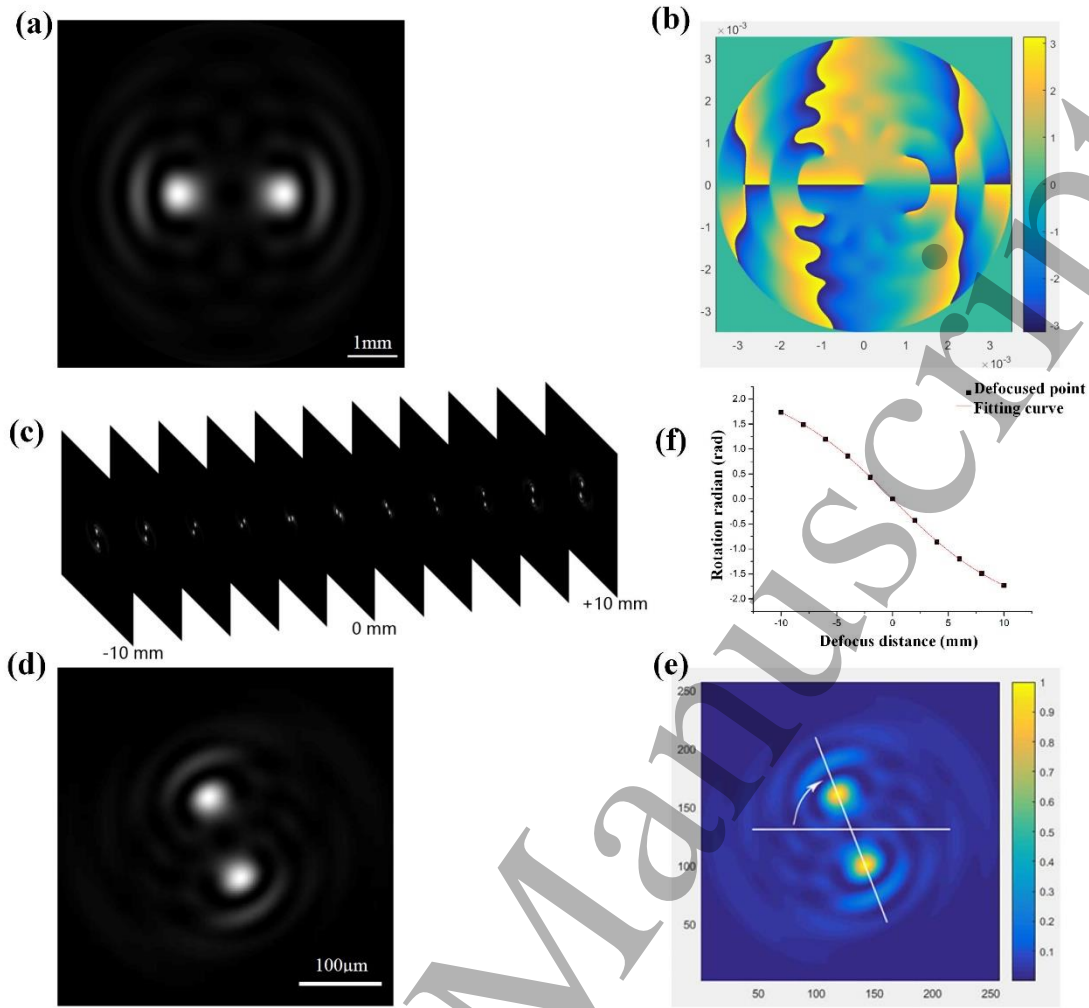


Figure 3. Numerical simulation of DH-PSF on original modulation function. (a) Amplitude modulation in the original modulation function, and (b) Phase modulation. (c) Defocus images obtained with the original modulation function. (d) Method to obtain the spot pair rotation angle: defocused image, and (e) Calculating inclination. (f) Variation of rotation with defocusing distance under the effect of the original modulation function.

The amplitude modulation diagram of the original modulation function shown in (Figure 3a) indicates that only a small portion of the optical channel in the imaging system allows light to pass freely. This means the utilization of light energy is low, which is not conducive to detecting weak signals. In practice, it is very difficult to produce an optical component capable of phase modulation and amplitude modulation simultaneously.

Therefore, a feasible alternative is to design the modulation function as a pure phase modulation function under the condition that the defocus double helix will not

be affected. This design ensures that the modulation function will not attenuate light within the scope of a clear aperture.

Set the amplitude modulation effect shown in (Figure 3a-b) to a constant to obtain a pure phase modulation function as shown in (Figure 4a-b). In Fig. 4(a), the entire aperture range is white, indicating that the entire channel allows free passage of light. As a result, the light-passing rate is improved by a factor 3.79 compared with the original modulation function.

The simulation was performed again using pure phase modulation. Images of a point source corresponding to different defocus distances are shown in (Figure 4c). When pure phase modulation is used, the system still turns the point light source into a spot pair, which rotates around its centre as the defocus distance changes.

The rotation angle for the spot pairs obtained using the original modulation function and those for spot pairs obtained using the pure phase modulation function are plotted on the same graph for comparison, as shown in (Figure 4d). When the pure phase modulation function is used, the system still exhibits a defocused double helix. When the point source moves in the positive direction along the optical axis, the spot pair rotates clockwise with an angle very similar to that produced by the original modulation function.

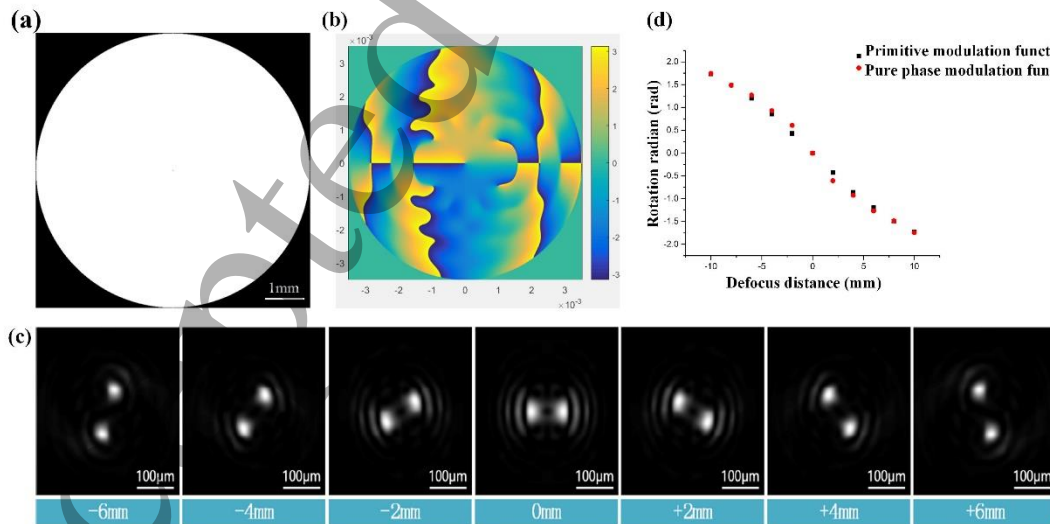


Figure 4. Numerical simulation of DH-PSF on pure phase modulation function. (a) Amplitude modulation of pure phase modulation function, and (b) Phase modulation. (c) Defocus images obtained with pure phase modulation. (d) Defocus curve of the primitive modulation function and pure phase modulation function.

3.2. Experimental verification of DH-PSF

A phase mask is an optical element formed from a transparent medium and designed with varying thickness to modulate the phase of light passing through it. An example is shown in **(Figure 5a)**, where light propagates from left to right. Points B and A are on the same light propagation surface for a medium with refractive index n . When light propagates to this surface, the beam at point B has travelled a distance Δd longer than the beam at point A in the medium. Therefore, the phase delay at point B relative to point A is

$$\frac{2\pi(n-1)\Delta d}{\lambda} \quad (21)$$

where n is the refractive index of the medium and λ is the wavelength (m).

The thickness map of the phase mask corresponding to pure phase modulation was calculated using Eq. (21). The phase mask was fabricated on a fused silica substrate with a diameter of 50 mm at the Chinese Academy of Sciences Shanghai Institute of Optics and Fine Mechanics. The fabricated phase mask is shown in **(Figure 5b)**.

An experimental light path shown in **(Figure 5c)** was designed based on the 4f system shown in **(Figure 2a)**. A parallel beam from a laser generator is first concentrated with a lens and is subsequently filtered with a small hole to remove high-frequency clutter before being used to simulate a point source. The laser generator and spatial light filter move in the axial direction to simulate the defocusing effect of a point source. The designed phase mask is placed at the position of the Fourier transform spectrum plane, and an imaging CCD is placed in the image plane for image acquisition.

To simplify the optical path and make the experiment more convenient, the laser generator is used to directly simulate the point source. The camera used in the experiment was a GEPER-B1020 (IMPERX, USA). Its resolution is of the order of a few million pixels with a pixel size of $5.5\mu\text{m}$, and the exposure time ranges from $2\mu\text{s}$ to 16ms .

The optical path was built on an optical plate. As shown in **(Figure 5d)**, the optical devices were mounted and adjusted along the broken line (optical axis). The laser generator was fixed along the optical path on a dovetail mobile platform, which could move along the optical axis to create the defocusing effect of a point source. The polarizing plate served to attenuate laser light so as to avoid damaging the photosensitive element in the camera. The diaphragm is mainly used to limit the size of the aperture so that the aperture matches the effective scope of the phase mask.

If the aperture is not limited by the diaphragm in the experiment, some light will reach the CCD directly without modulation in advance, which will hinder formation of a spot pair and affect the experimental result.

Before conducting the experiment, the phase mask was removed from the optical path and an optical whiteboard was placed in front of the CCD. The two polarizing plates were adjusted to obtain the appropriate light intensity. After that, the optical whiteboard was removed so that an image could form on the CCD. The position of the laser generator was fine-tuned along the optical axis while the end image was observed. When the spot size reached a minimum, the corresponding laser generator position was set to zero, i.e., the defocus distance was zero at this position.

(Figure 5e) shows defocus images with and without the phase mask, where the defocus distance was varied from -6 mm to +6 mm in 2 mm intervals. When the phase mask was not used, the end image of the point source was an expanded spot, and the spot diameter increased as the defocus distance deviated from zero. The point light source was projected as a spot pair when the phase mask was used. The spot rotated clockwise around its center when the point source was moved in the positive direction along the optical axis, which is consistent with the simulation result.

The defocused double helix images were processed to obtain their rotation angles. The experimental data was compared with the simulation data shown in **(Figure 5f)**. Due to the tolerances of the optical components, installation position, and phase mask processing, discrepancies exist between the experimental data and the simulation data. However, it can be said that the experimental data agrees well with the simulation

data (the average discrepancy being 4%).

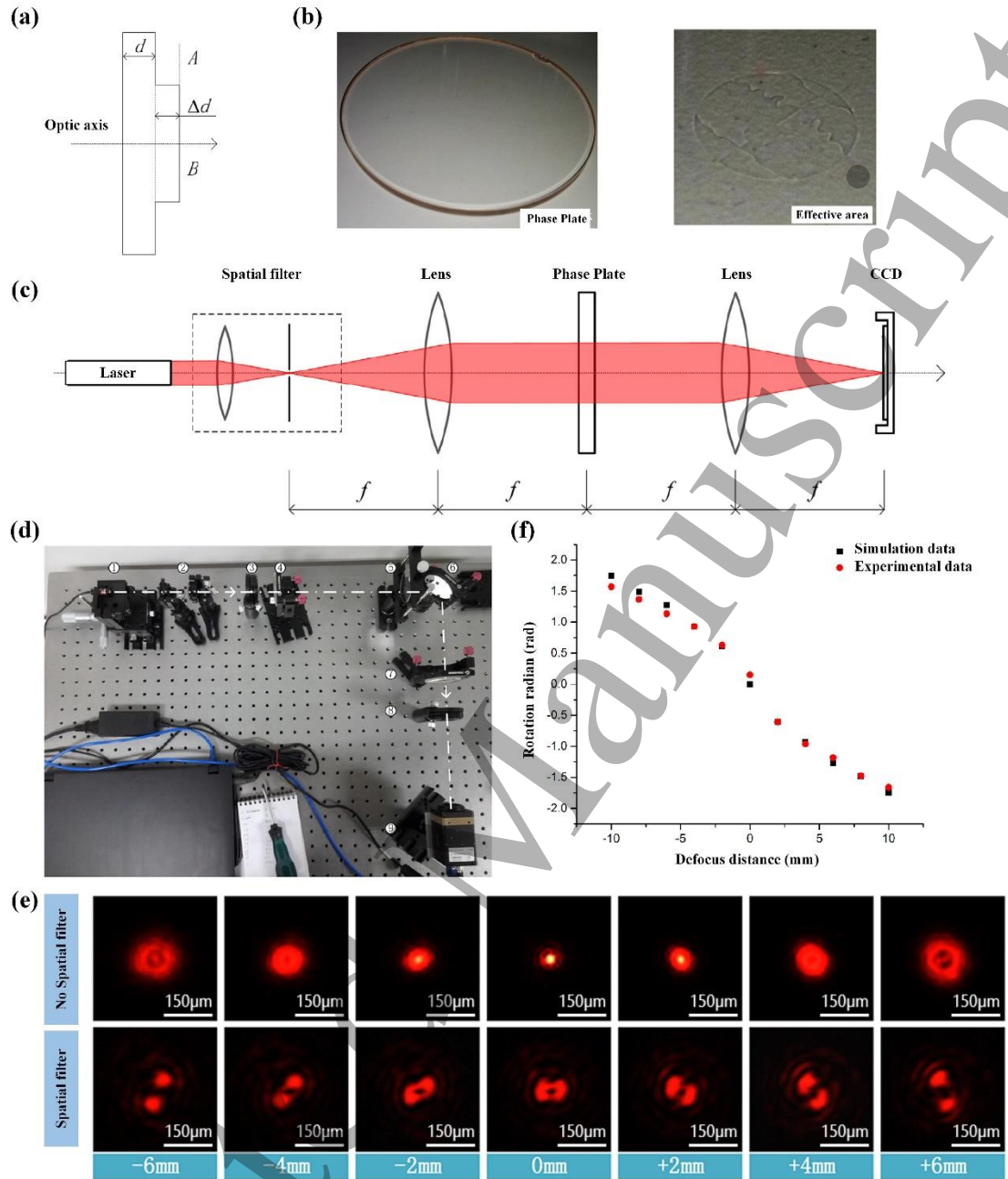


Figure 5. Experimental verification of DH-PSF. (a) Example of phase mask design. (b) A phase mask designed and produced for experiment. (c) Schematic of the optical path in the defocused double helix experiment. (d) Optical path in the defocused double helix experiment: ①Laser generator ②Polarizing plate ③diaphragm ④Lens ⑤Phase mask ⑥Mirror ⑦Lens ⑧Diaphragm ⑨Camera. (e) Comparison of defocused images. (f) Comparison of simulation and experimental data.

4. Results and discussion

4.1. Construction of a QD nanoscale 3D localization and temperature measurement system

The core of the QD 3D localization system is a DH-PSF whose function is to convert the defocus distance of the QD into a rotation angle for the spot pair, followed by determining the relative position of the QD according to the rotation angle. The QDs are magnified with the microscopic imaging system and projected on the focal plane of the positioning system. When magnifying the QDs, the microscopic imaging system will also magnify the defocus distance with a magnification of approximately the square of the transverse magnification. When an objective lens with magnification of 100x is used, a QD with 10nm diameter and 1 μ m away from the focus will be projected into an image whose with 1 μ m diameter located 10mm from the image focus.

4.1.1. Design of the thermal imaging system

The QD temperature measurement and positioning system designed in this study is shown in **(Figure 6a)**. The microscopic imaging system (①) is located in the middle of the system. The QD fluorescence image is fed to the QD fluorescence temperature measurement system (②) and the QD 3D positioning system (③) to fulfil the functions of temperature measurement and QD spatial positioning. Interested readers are referred to a previous publication for details of the QD temperature measurement system.^[40]

The microscope used in this study was an infinity optical system shown in **(Figure 6b)**. In an infinity optical system, the objective lens will collimate rays from the object. Another fixed tube lens will focus the collimated rays to the focal plane of the ocular lens.

The objective lens of the microscopic imaging system used in this study was an Olympus UPLSAPO 100XO. The above system was simplified to a finite conjugation microscope system according to the Olympus component selection manual, as shown in **(Figure 6c)**. The equivalent focal length f was 2.205 mm, the object focal length l

was 22.05 μm , and the image focal length L was 220.5 mm.

4.1.2. Design of QD spatial positioning system

The QD positioning system shown in **(Figure 6d)** was designed and constructed based on **(Figure 5d)**. The system is capable of performing 3D (axial and transverse) positioning. The dotted line in the figure shows the optical path. The beam from the microscopic imaging system passes through ① lens, ② diaphragm, ③ filter, ④ phase mask, ⑤ mirrors, ⑥ lens, ⑦ diaphragm, and finally forms an image on ⑧ camera.

The camera used in the system was iXon Ultra 888 from Andor, UK. The camera was an EMCCD camera with a resolution on the order of a few million pixels and a pixel size of 13 μm . Given the camera's sensor size and the magnification of the objective lens, the field of view was calculated as $133 \times 133 \mu\text{m}^2$. The positioning resolution of the QDs in the XY plane was 130nm. Since the pixel size in the photosensitive element was 1 μm , and the system used a microscope objective lens with 100x magnification, the theoretical positioning accuracy in the transverse dimension is 10nm.

The transverse magnification of the microscope was using images of a micrometer. The distance between pixels was compared to the micrometer scale. A TK908 microscope micrometer was used for calibration. A $1 \times 1 \text{ mm}^2$ was divided into 100×100 grids with 0.01mm grid spacing.

During the experiment, the operator placed the micrometer on the object platform and observed the image of the micrometer with the ocular lens. Then, the operator fine-tuned the working distance of the ocular lens until the image became clear. The position of the micrometer was adjusted so that a large number of grid units could be observed in the field of view. The operator then removed the phase mask in the QD 3D positioning system and used the EMCCD to acquire the image, as shown in **(Figure 6e)**.

The operator marked the length of 10 grid units and calculated the number of pixels in this section, as shown in **(Figure 6f)**. The calibration results show that the

actual size of each image pixel was 0.128 μ m.

Axial calibration was performed to obtain the relationship between the defocus distance and the rotation angle. Since the micro-displacement platform was very expensive, calibration was carried out using theoretical simulations. According optical theory, the transverse amplification β of the system shown in (Figure 6c) is:

$$\beta = \frac{L}{f} = \frac{f}{l} \quad (22)$$

where L is image focal length (m), f is lens focal length (m), and l is the object distance (m).

When the object shifts a distance Δl , its conjugate image will also shift by

$$\Delta L = \frac{f^2}{l + \Delta l} - L \quad (23)$$

A string of ΔL values were calculated using Eq. (23), each corresponding to a value of Δl ranging from -660nm to +700nm in 10nm intervals. The rotation angles of the spot pair at different defocus distances were calculated. The results are plotted in (Figure 6g). The curve can be divided into three sections, and each section can be approximated as a straight line, indicating a linear correlation. Therefore, the curve can be fitted into the three section curve shown in (Figure 6h) and Table 2.

Table 2. Section-wise fitting results

Defocus distance (nm)	Rotation radian (rad)	Fitting equation
-660~-150	0.5586~1.544	$\theta = 0.2689 - 0.001932\Delta l$
-150~150	-0.5586~-0.5586	$\theta = -0.003723\Delta l$
150~700	-1.544~-0.5586	$\theta = -0.2896 - 0.001792\Delta l$

The spacing between light spots on the image plane increases with increased defocus distance, thus the axial positioning resolution increased as the defocus distance increased. The simulation result shows that when the point source is located in the focal plane at the object side, the spacing of the light spots is 78 μ m, which corresponds to 6 pixel spaced. The corresponding rotation angle resolution is $\frac{\pi}{6}$, and the corresponding axial positioning resolution is 140nm.

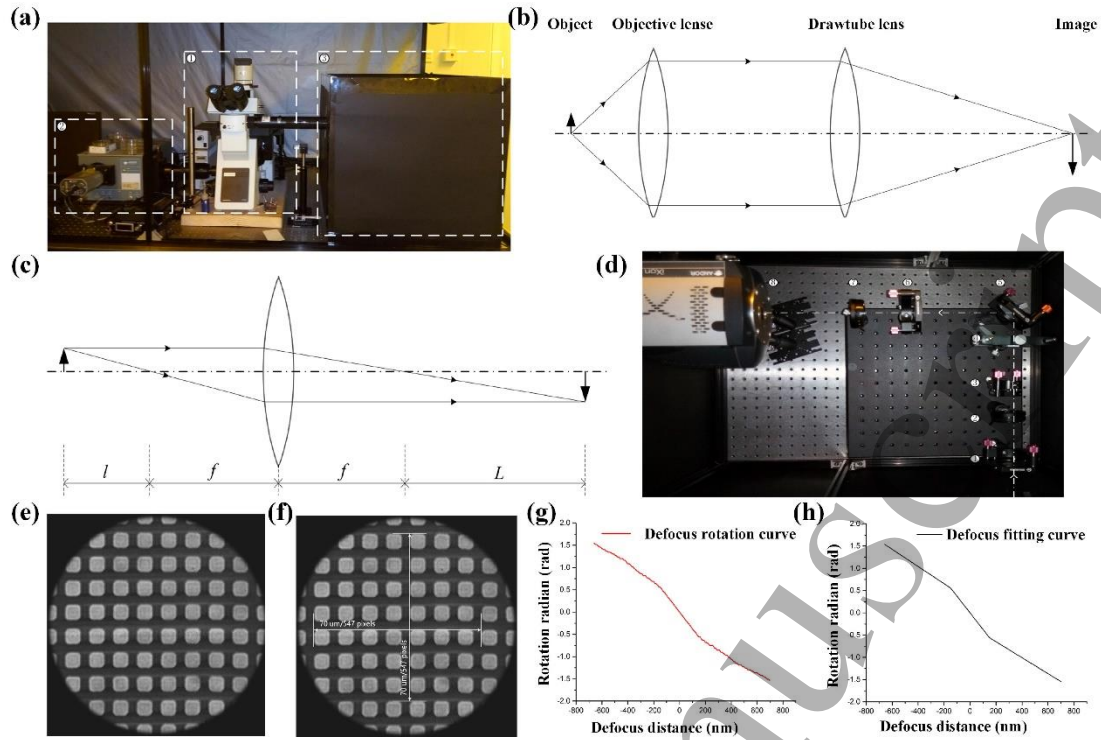


Figure 6. Construction of a QD nanoscale 3D localization and temperature measurement system. (a) QD temperature measurement and positioning system. ① Microscopic imaging system ② QD fluorescence temperature measurement system ③ QD 3D positioning system. (b) Optical path of collimated rays. (c) Equivalent finite conjugation microscopy system. (d) QD 3D positioning system. ① lens, ② diaphragm, ③ filter, ④ phase mask, ⑤ mirrors, ⑥ lens, ⑦ diaphragm, and ⑧ camera. (e) Image of a micrometer: original image, and (f) Processed image. (g) Defocus rotation curve: defocus-rotation curve Defocus distance, and (h) Fitted defocus-rotation curve.

4.2. Experimental Section

Synthesis of QDs for thermal sensing: Details of the synthesis process were reported in the literature. Typically, 4 ml of 0.04 mol/L CdCl_2 was first diluted to 50 ml with ultrapure water and placed in a three-necked flask. Next, 100 mg sodium citrate, 4 ml of 0.01 mol/L Na_2TeO_3 solution, 50 mg mercaptosuccinic acid (MSA) and 50 mg NaBH_4 were successively added under constant stirring. When the solution color turned yellow-green, nitrogen gas was introduced then the flask was condensed and refluxed several times at 100 ° C to obtain CdTe quantum dots with different particle sizes and fluorescence properties.

Co-culture of QDs and living liver cancer cells: The liposome transfection method was employed for the QD intake, in which liposomes were used as vehicles to transfer the QDs into cells. 50 liver cancer cells were incubated and the culture media was changed every 1–2 days. After that, a 1 mL cell suspension with 1.0×10^5 cells was sub-cultured in a 20 mm confocal Petri dish, followed by incubation for a period of 10 h. At this point, QDs with the appropriate concentration were added for loading using a Lipofectamine 2000 Reagent kit.

4.3. Detection of temperature field in tumour cells

A cell experiment was designed to measure the temperature and spatial position of the QDs simultaneously. A QD probe was fabricated, and the relationship between temperature and peak wavelength was obtained through a calibration experiment. The object of the experiment was to verify the capability of the system for measuring temperature at the micro-nano scale.

An inverted fluorescence microscope was used to monitor the internalization of QDs into cells and the images were captured and shown in (Figure 7). From (Figure 7a), the image of cells swallowed with QDs was acquired under white light mode. (Figure 7b) is the picture under fluorescence excitation mode. The picture shown in (Figure 7c) is a combination of the aforementioned two pictures.

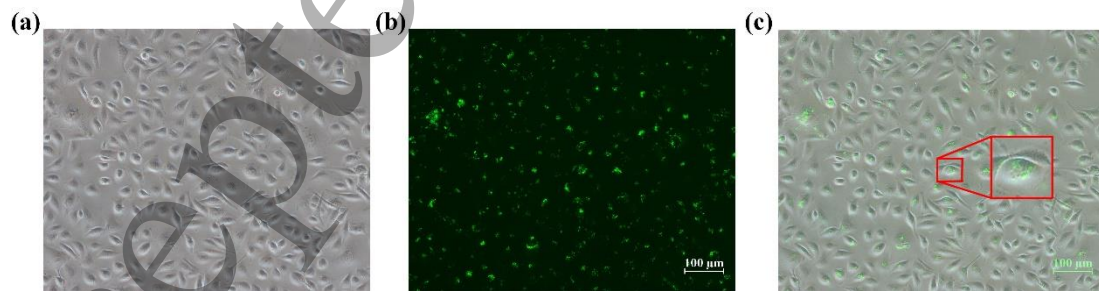


Figure 7. Cell images after QDs uptake under. a) White light. b) Ultraviolet wave band excitation light. c) Combined the picture of (a) and (b).

There were so many quantum dots around the cell. For convenience, eight QDs were identified in the region with a low concentration surrounding the cell, as shown

in (Figure 8a-b).

The image center was taken as the origin in the XY plane for positioning. The brightest QDs were connected, and the transverse position of a spot pair was determined according to the midpoint coordinates of the connection line and the transverse calibration result. The axial position was determined from the inclination of the connection line and the axial calibration result, as shown in Table 3.

Table 3. Spatial location of quantum dots

Quantum dot No.	Rotate radian (rad)	Spatial location (X,Y,Z)
1	0.3174	(-7.24 μm , -4.01 μm , -85nm)
2	0.8079	(-1.96 μm , -5.38 μm , -279nm)
3	0.4304	(2.15 μm , -4.20 μm , -116nm)
4	1.0272	(9.52 μm , -0.57 μm , -392nm)
5	-0.4588	(-7.35 μm , 1.06 μm , 123nm)
6	0.5124	(1.26 μm , 0.39 μm , -138nm)
7	-0.2807	(5.30 μm , -1.14 μm , 75nm)
8	-0.9465	(1.98 μm , 4.97 μm , 367nm)

The temperature controller was set to 65 °C, and the QD fluorescence spectrum was measured with a spectrometer.^[40] The spectral data are recorded every 60 seconds, and the temperatures of eight QDs is calculated according to the functional relationship between wavelength and temperature, as shown in Table 4. (Figure 8c) shows the fluorescence spectrum of QD ① as the temperature rose. As the temperature rose, the peak fluorescence wavelength from QD ① became longer, and the fluorescence intensity became weaker. The peak wavelength and temperature curve for QD ① are shown in (Figure 8d).

Table 4. Temperature and Wavelength of quantum dots

Time	QD①		QD②		QD③		QD④		QD⑤		QD⑥		QD⑦		QD⑧	
	λ/nm	$T/^\circ\text{C}$	λ/nm	$T/^\circ\text{C}$	λ/nm	$T/^\circ\text{C}$	λ/nm	$T/^\circ\text{C}$	λ/nm	$T/^\circ\text{C}$	λ/nm	$T/^\circ\text{C}$	λ/nm	$T/^\circ\text{C}$	λ/nm	$T/^\circ\text{C}$
0s	534.67	23.85	543.73	24.22	543.53	23.06	543.63	23.66	543.75	24.36	543.90	25.25	543.80	24.57	543.61	23.47
60s	544.14	26.60	544.17	26.84	543.99	25.74	544.05	26.12	543.02	25.84	544.21	27.02	544.42	28.31	543.87	25.00

1																	
2																	
3																	
4	120s	544.58	29.14	544.53	28.96	544.42	28.32	544.61	29.38	544.58	29.21	544.62	29.41	544.76	30.26	544.40	28.10
5																	
6	180s	544.83	30.68	544.79	30.47	544.90	31.10	544.92	31.24	544.99	31.57	544.01	31.69	545.14	32.54	544.83	30.72
7																	
8	240s	545.30	33.52	545.20	32.89	545.23	33.08	545.36	33.76	545.29	33.34	545.44	34.23	545.30	33.45	545.14	32.53
9																	
10	300s	545.58	35.02	545.76	36.15	545.54	34.87	545.77	36.20	545.70	35.79	545.81	36.43	545.44	34.30	545.30	33.45

11
12 Based on the experimental data, we process the information of quantum dots and
13 reconstruct the schematic diagram of the temperature field of hepatocellular
14 carcinoma cells as shown in (**Figure 8e**). In the initial stage, $t=0$ s, we collect a lot of
15 information about quantum dots, including temperature and location. The initial
16 temperature of the probes is about 24 °C, but their positions are randomly distributed.
17 In order to facilitate the plotting, we only extract some quantum dots' data and
18 reconstruct the temperature distribution of hepatocellular carcinoma cell clusters by
19 synthesizing information. The color of quantum dots represents its temperature value.
20 The color changes from dark blue to dark red, and the corresponding temperature
21 range ranges from 20 °C to 40 °C. Because temperature changes slowly, we re-collect
22 data every 60 seconds. In order to facilitate the reader's observation, we further
23 reduced the number of quantum dots, but only highlighted the thermal imaging maps
24 of eight quantum dots. As the heating process continues, it can be observed from
25 (**Figure 8e**) that the color of quantum dots changes slowly and redshifts gradually,
26 which indicates that the temperature of quantum dots increases gradually. It also
27 means that the temperature of cells corresponding to quantum dots increases gradually.
28 Among them, the temperature of quantum dot 6 is the highest, with a value of 36.4 °C,
29 and the quantum dot 4 temperature increases the most, with a temperature increase of
30 12.6 °C compared with the initial temperature.

31
32 As far as we know, this is the first time that the academia has succeeded in
33 simultaneous tracking and temperature measurement of quantum dots. The proposed
34 method will have a wide range of applications. If applied to cell research, it can locate
35 and track the trajectory of key substances in metabolism. If enough quantum dots are
36 melted into cells, accurate measurement of thermal imaging and temperature gradient
37 distribution in micron cells can be achieved. Through accurate 3D temperature
38
39
40
41
42
43
44
45
46
47
48
49
50
51
52
53
54
55
56
57
58
59
60

measurement at the micro-nano scale, researchers can establish the relationship between local heat generation and metabolic processes, which allows them to identify the causes of various diseases.

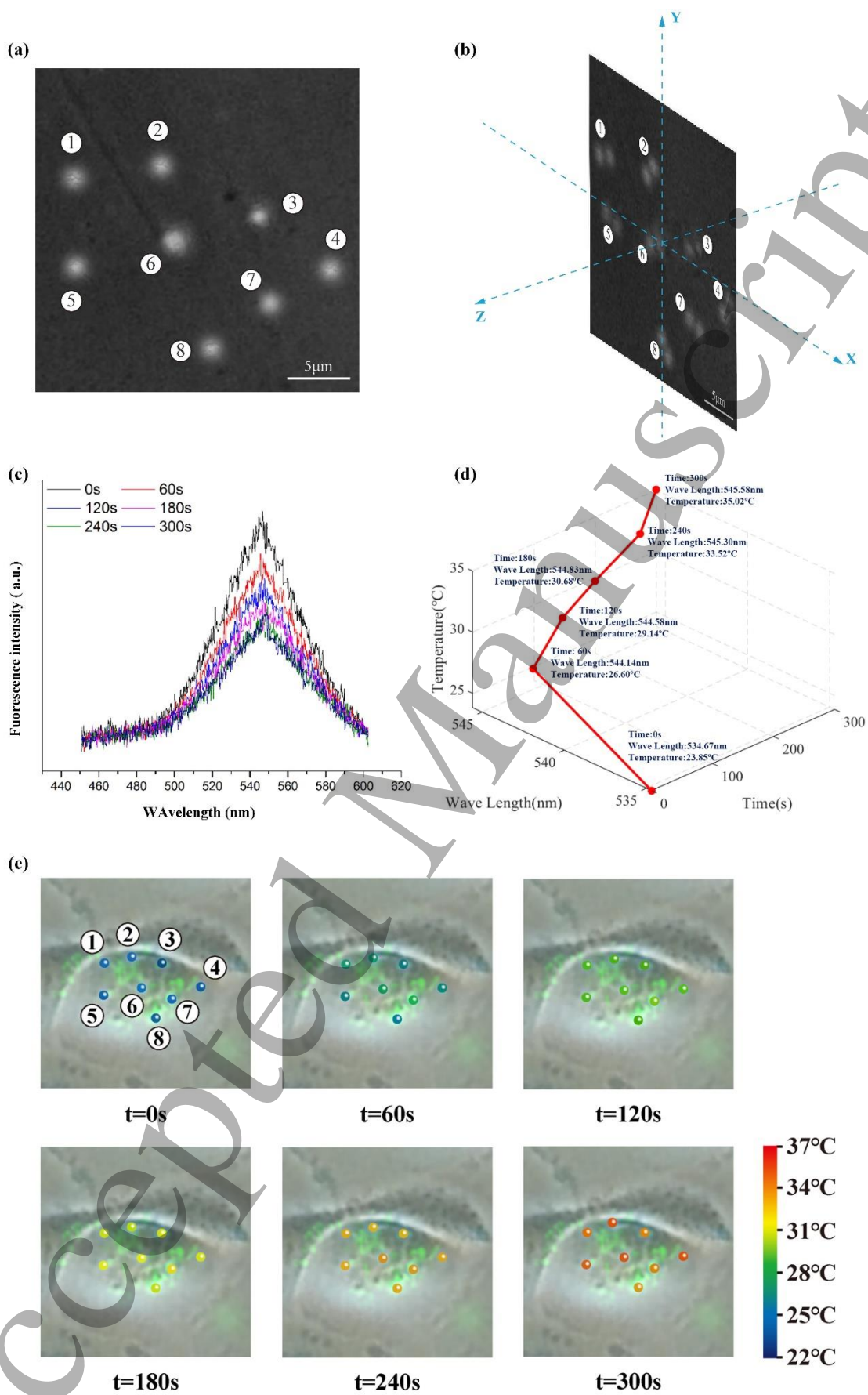


Figure 8. Three-dimensional temperature field imaging of tumor cells. (a) Imaging of QDs in a low

density area: ordinary QD imaging, and (b) QD double helix imaging. (c) Spectrum and temperature curve of QD①: Fluorescence spectrum, and (d) Peak wavelength and temperature. (e) Restructuring graph of three-dimensional temperature field of tumor Cells at 0s, 60s, 120s, 180s, 240s and 300s.

5. Conclusion

A 3D positioning method was developed in this study to meet the challenge of tracking the spatial position of particles at the micro-nano scale. The generation and propagation of vortex beams were analyzed, and the formation of the DF-PSF was derived. An imaging system model based on a 4f system was constructed, and the appropriate imaging parameters (lens focal length: 200 mm; clear aperture: 7 mm) were determined. A DH-PSF was designed using a spectrum plane modulation function obtained via superposition of the Laguerre-Gaussian mode group (1, 0), (3, 1), (5, 2), (7, 3), and (9, 4) with 1.0 mm beam waist. A QD 3D positioning system was constructed with a phase mask as an optical modulator, $133 \times 133 \times 1.36 \mu\text{m}^3$ measurement range, and a spatial positioning resolution of approximately 140nm. The experimental results show that the experimental optical path fulfilled its designed function. The system was developed by combining a 3D positioning technique with a quantum temperature measurement technique. We applied the system in the field of cell temperature measurement. For the first time, we realized three-dimensional positioning and temperature measurement of quantum dot probes at nanoscale and reconstructed the temperature field of cells. The method proposed in this paper can be applied in the field of cell thermal metabolism for accurately plotting 3D temperature field gradient maps of cells in real time. This paves the way for establishing the correlation between metabolism and heat, thereby improving the accuracy and reliability in tumour diagnosis and new drug trials.

Acknowledgments

This work was financially supported by the National Natural Science Foundation of China (No. 51605375), Natural Science Foundation of Shaanxi (No.2017JM5081) , the China Postdoctoral

Science Foundation (No. 2017T100741), The Central Universities fundamental research funds (No. xjj2017164).

Conflict of interest

The authors declare no conflict of interest.

References

- [1] Mathai P. P, Liddle J. A, Stavitskiy S M. Optical tracking of nanoscale particles in microscale environments [J]. *Applied Physics Reviews*, 2016, 3(1), DOI: 10.1063/1.4941675.
- [2] Shen Hao, Tauzin Lawrence J, Baiyasi Rashad. Single Particle Tracking: From Theory to Biophysical Applications[J]. *Chemical Reviews*, 2017, 117(11): 7331-7376.
- [3] Beaune G, Dubertret B, Clément O, et al. Giant vesicles containing magnetic nanoparticles and quantum dots: feasibility and tracking by fiber confocal fluorescence microscopy[J]. *Angewandte Chemie International Edition*, 2007, 46 (28): 5421-5424.
- [4] Bon P, Linares L J, Feyeux M, et al. Self-interference 3D super-resolution microscopy for deep tissue investigations [J]. *Nature Methods*, 2018, 15(6):449 . DOI: 10.1038/s14592-018-0005-3.
- [5] Smoyer Christine J, Katta Santharam S, Gardner Jennifer M, et al. Analysis of membrane proteins localizing to the inner nuclear envelope in living cells [J]. *Journal of Cell Biology*, 2016, 215(4): 575-590.
- [6] Liu, Wei; Liu, Si-Jia; Kuang, Yong-Qing. Developing Activity Localization Fluorescence Peptide Probe Using Thiol-Ene Click Reaction for Spatially Resolved Imaging of Caspase-8 in Live Cells [J]. *Analytical Chemistry*, 2016, 88(15): 7867-7872.
- [7] Johnson CK , Harms GS. Tracking and localization of calmodulin in live cells [J]. *Biochimica Et Biophysica Acta- Molecular Cell Research*, 2016, 1863(8): 2017-2026.
- [8] Ballister Edward R, Aonbangkhen Chant, Mayo Alyssa M. Localized light-induced protein dimerization in living cells using a photocaged dimerizer [J]. *Nature Communication*, 2014, 5, DOI: 10.1038/ncomms6475.
- [9] Wells NP, Lessard GA, Werner JH. Confocal, 3-dimensional tracking of individual quantum dots in high background environments[J]. *Analytical chemistry*, 2008, 80 (24): 9830.
- [10] Liu Hong Wen, Li Ke, Hu Xiao Xiao, et al. In Situ Localization of Enzyme Activity in Live Cells by a Molecular Probe Releasing a Precipitating Fluorochrome [J]. *Angewandte Chemie - International Edition*, 2017, 56(39): 11788-11792.
- [11] Huang Kun, Doyle Francis, Wurz Zachary E, et al. FASTmiR: an RNA-based sensor for in vitro quantification and live-cell localization of small RNAs [J]. *Nucleic Acids Research*, 2017, 45(14), DOI: 10.1093/nar/gkx504.
- [12] Hu C, Wong CM, Xu CS, et al. Confocal three dimensional tracking of a single nanoparticle

- with concurrent spectroscopic readouts[J]. *Applied Physics Letters*, 2006, 88 (22): 223901-223901-223903.
- [13] Parthasarathy R. Rapid, accurate particle tracking by calculation of radial symmetry centers[J]. *Nature Methods*, 2012, 9 (7): 724-726.
- [14] Speidel M, Jonáš A, Florin E-L. Three-dimensional tracking of fluorescent nanoparticles with subnanometer precision by use of off-focus imaging[J]. *Optics letters*, 2003, 28 (2): 69-71.
- [15] Zhang Z, Menq C-H. Three-dimensional particle tracking with subnanometer resolution using off-focus images[J]. *Applied optics*, 2008, 47 (13): 2361-2370.
- [16] van Loenhout MT, Kerssemakers JW, De Vlaminck I, et al. Non-bias-limited tracking of spherical particles, enabling nanometer resolution at low magnification[J]. *Biophysical journal*, 2012, 102 (10): 2362-2371.
- [17] Zhang Z, Menq C-H. Best linear unbiased axial localization in three-dimensional fluorescent bead tracking with subnanometer resolution using off-focus images[J]. *JOSA A*, 2009, 26 (6): 1484-1493.
- [18] Marki A, Ermilov E, Zakrzewicz A, et al. Tracking of fluorescence nanoparticles with nanometre resolution in a biological system: assessing local viscosity and microrheology[J]. *Biomechanics and modeling in mechanobiology*, 2014, 13 (2): 275-288.
- [19] Pereira F, Gharib M. Defocusing digital particle image velocimetry and the three-dimensional characterization of two-phase flows[J]. *Measurement Science and Technology*, 2002, 13 (5): 683.
- [20] Carr A R, Ponjavic A, Basu S. Three-Dimensional Super-Resolution in Eukaryotic Cells Using the Double-Helix Point Spread Function[J]. *Biophysical Journal*, 2017, 112(7):1444 - 1454.
- [21] Pavani SRP, Thompson MA, Biteen JS, et al. Three-dimensional, single-molecule fluorescence imaging beyond the diffraction limit by using a double-helix point spread function[J]. *Proceedings of the National Academy of Sciences*, 2009, 106 (9): 2995-2999.
- [22] Shechtman Yoav, Gustavsson ANNA Karin, Petrov Petar N, et al. Observation of live chromatin dynamics in cells via 3D localization microscopy using Tetrapod point spread functions [J]. *Biomedical Optics Express*, 2017, 8(12): 5735-5748.
- [23] Thompson MA, Casolari JM, Badieirostami M, et al. Three-dimensional tracking of single mRNA particles in *Saccharomyces cerevisiae* using a double-helix point spread function[J]. *Proceedings of the National Academy of Sciences*, 2010, 107 (42): 17864-17871.
- [24] Greengard A, Schechner YY, Piestun R. Depth from diffracted rotation[J]. *Optics letters*, 2006, 31 (2): 181-183.
- [25] Jaiswal JK, Mattoussi H, Mauro JM, et al. Long-term multiple color imaging of live cells using quantum dot bioconjugates[J]. *Nature biotechnology*, 2003, 21 (1): 47-51.
- [26] Medintz IL, Uyeda HT, Goldman ER, et al. Quantum dot bioconjugates for imaging,

- labelling and sensing[J]. *Nature materials*, 2005, 4 (6): 435-446.
- [27] Nozik A. Quantum dot solar cells[J]. *Physica E: Low-dimensional Systems and Nanostructures*, 2002, 14 (1): 115-120.
- [28] Kim T-H, Cho K-S, Lee EK, et al. Full-colour quantum dot displays fabricated by transfer printing[J]. *Nature photonics*, 2011, 5 (3): 176-182.
- [29] Bae WK, Kwak J, Lim J, et al. Multicolored light-emitting diodes based on all-quantum-dot multilayer films using layer-by-layer assembly method[J]. *Nano letters*, 2010, 10 (7): 2368-2373.
- [30] Liu Rongjun, Zhao Jingjin, Huang Zirong, et al. Nitrogen and phosphorus co-doped graphene quantum dots as a nano-sensor for highly sensitive and selective imaging detection of nitrite in live cell [J]. *Sensors and Actuators B-Chemical*, 2017, 240:604-612.
- [31] Mu Xiaoyu, Wang Jun-Ying, Bai Xueting, et al. Black Phosphorus Quantum Dot Induced Oxidative Stress and Toxicity in Living Cells and Mice [J]. *ACS Applied Materials & Interfaces*, 2017, 9(24): 20399-20409.
- [32] Ma Yingxin, Wang Mingxiu, Li Wei, et al. Live cell imaging of single genomic loci with quantum dot-labeled TALEs [J]. *Nature communications*, 2017, 8. DOI: 10.1038/ncomms15318.
- [33] Choudhury D, Jaque D, Rodenas A, et al. Quantum dot enabled thermal imaging of optofluidic devices[J]. *Lab on a Chip*, 2012, 12 (13): 2414-2420.
- [34] Pugh-Thomas D, Walsh BM, Gupta MC. CdSe (ZnS) nanocomposite luminescent high temperature sensor[J]. *Nanotechnology*, 2011, 22 (18): 185503.
- [35] Li S, Zhang K, Yang J-M, et al. Single quantum dots as local temperature markers[J]. *Nano letters*, 2007, 7 (10): 3102-3105.
- [36] Piestun R, Schechner YY, Shamir J. Propagation-invariant wave fields with finite energy[J]. *JOSA A*, 2000, 17 (2): 294-303.
- [37] An Gang. Point spread function of CCD optical imaging system and its application in sub-pixel edge location [D] : Jilin University, 2008.
- [38] Wang Xue. Research on the image processing of 4f optical system spot based on CCD [D]: Heilongjiang University, 2015.
- [39] Cui Longxie. 4f Optical Information Processing System [J]. *Journal of North China Electric Power College*, 1995, 22 (1): 97-102.
- [40] Jiang Xinbing, Ben Q. Li, Xiaoli Qu, et al. Thermal sensing with CdTe/CdS/ZnS quantum dots in human umbilical vein endothelial cells [J]. *Journal of Materials Chemistry B*, 2017, 5(45):8983-8990.